

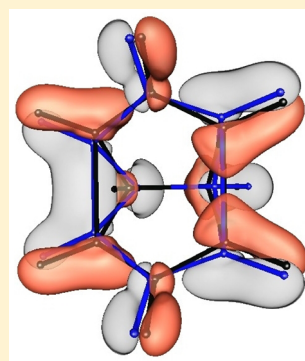
Electron–Nuclear Motion in the Cope Rearrangement of Semibullvalene: Ever Synchronous?

Timm Bredtmann* and Beate Paulus

Institut für Chemie und Biochemie, Freie Universität Berlin, Takustr. 3, 14195 Berlin, Germany

S Supporting Information

ABSTRACT: The effect of nuclear motion on the synchronicity of the pincer motion type electronic rearrangement associated with bond making and bond breaking and vice versa is investigated for the degenerate Cope rearrangement of semibullvalene using a time-independent quantum chemical approach. We find that distinct paths along the potential energy surface corresponding to synchronous nuclear rearrangement involve asynchronous electronic fluxes out of the old and into the new bond while synchronous electronic fluxes entail asynchronous nuclear rearrangement. In order to demonstrate the robustness of the results, various high-level quantum chemical methods including full structure optimizations up to second order multireference perturbation theory using triple- ζ basis sets (RS2/cc-pVTZ), which are subsequently refined at the RS3/cc-pVTZ and MRCI+Dav/cc-pVTZ levels of theory, are used for solving the electronic Schrödinger equation. These benchmark results extend previous quantum chemical data for the degenerate Cope rearrangement of semibullvalene and are tested against lower level methods (e.g., density functional theory calculations using the B3LYP and B3PW91 functionals).



INTRODUCTION

The degenerate [3,3]-sigmatropic shift (degenerate Cope rearrangement) of semibullvalene and its derivatives has been extensively studied both experimentally and theoretically since the first preparation of the parent compound in 1966 by Zimmerman et. al;^{1,2} see refs 3–13 and 10–26, respectively. These investigations focused mainly on its thermochromicity,^{6,8,9,12,15} as well as on the bishomoaromatic character of the transition state and its stabilization with respect to the reactant and product by appropriate substitution of the parent compound; see for example refs 10–12, 16, 18, 19, 22, 25 and ref 13 for a recent experimental realization of a bishomoaromatic ground state. Here, we focus on mechanistic details of this pericyclic reaction, in particular, on the synchronicity of the coupled electronic and nuclear motion associated with bond breaking and bond making. Such investigations are motivated by ongoing combined experimental and theoretical progress in monitoring electron–nuclear real-time dynamics from femto-to-attosecond time scales.^{27–33}

The degenerate Cope rearrangement of semibullvalene proceeds in a symmetric double well potential from the reactant with C_s -symmetry through a high symmetry species (HSS) with C_{2v} -symmetry to the product with C_s -symmetry, see Figure 1. There are three mechanistic extremes for the Cope rearrangement in general and the degenerate Cope rearrangement of semibullvalene in particular, which may be distinguished by the interallylic distance R (C_2 – C_8 , or equivalently the C_4 – C_6 , distance in the HSS; see Figure 1.^{25,34–38} More pronounced σ -bond elongation associated with carbon atoms C_2 and C_8 compared to σ -bond contraction associated with carbon atoms C_4 and C_6 leads to bis-allyl-like

structures with corresponding large interallylic distance R , while more pronounced σ -bond contraction compared to σ -bond elongation leads to 3,7-diyl-like structures with associated short R values. Finally, synchronous σ -bond elongation and contraction leads to bishomoaromatic structures with intermediate values of the interallylic distance R . This synchronicity of nuclear motion in pericyclic reactions has been intensively debated for almost three decades; see for example refs 39–43.

Recently, we investigated the analogous synchronicity of the electronic bond-to-bond fluxes accompanying synchronous nuclear rearrangement in terms of quantum dynamical simulations.^{21,23} We found that the pincer-motion type rearrangement of the electrons common to pericyclic reactions occurring in nondegenerate electronic states, such as the electronic ground state,⁴⁵ c.f. Figure 1, depends on the preparation of the reactant: the electronic bond-to-bond fluxes are expected to be synchronous in the case of tunneling at cryogenic temperatures and asynchronous when the reaction is induced by selective laser pulses.^{20,21,23,26} The latter scenario corresponds to the reaction from the reactant to the product at energies well above the barrier and was modeled at the B3LYP^{46,47} level of theory using the cc-pVTZ basis sets⁴⁸ assuming synchronous rearrangement of all the nuclei; see also ref 24 for a recent confirmation of our results.

Here, we extend our previous investigations on electronic fluxes over the potential barrier within a time-independent quantum chemical treatment exploring various paths along the potential energy surface (PES) from the reactant over specific

Received: April 18, 2013

Published: May 20, 2013

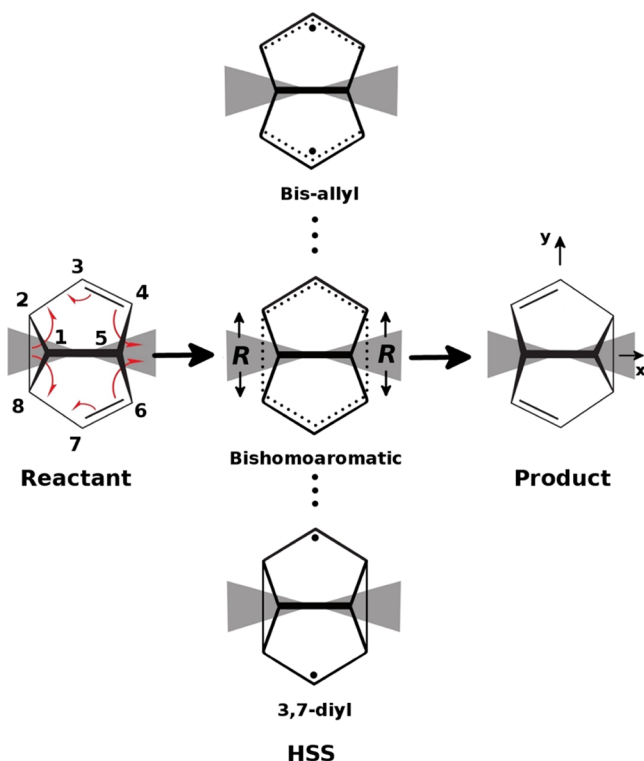


Figure 1. Sketch of the degenerate Cope rearrangement of semibullvalene from the reactant (C_s -symmetry) through distinct high symmetry species (HSS, C_{2v} -symmetry), which may be distinguished by the interallylic distance R to the product (C_s -symmetry). The origin of the coordinate system is chosen as the center of mass, and the axes are eigenvectors of the inertia tensor.⁴⁴ Additionally shown are the sectors used to monitor the pincer-motion type electronic flux common to pericyclic reactions occurring in the electronic ground state⁴⁵ out of the old and into the new bond as gray shaded areas left and right of the center of mass, respectively.

HSS covering the extremes shown in Figure 1 to the product at different levels of theory going beyond density functional theory (DFT) to investigate the robustness of the previously reported counterintuitive results. These investigations include a test of the observer planes used to monitor the electronic rearrangement. In particular, full RS2/cc-pVTZ^{49,50} structure optimizations are performed in C_s -symmetry and in C_{2v} -symmetry for the transition state as well as along a particular path involving synchronous σ -bond elongation and σ -bond contraction. Additionally, special emphasis is laid on the adequacy of the quantum chemical method to describe the continuum between radical and homoaromatic HSS. For this purpose, we study a C_{2v} -cut through the PES as a function of the interallylic distance R with all other degrees of freedom optimized at the RS2/cc-pVTZ level including a refinement at the RS3/cc-pVTZ⁴⁹ and MRCISD+Dav/cc-pVTZ^{51–53} levels of theory; see refs 16 and 18 for an analogous treatment focusing solely on the stationary points and using RS2 single point calculations on CASSCF^{54,55} and B3LYP optimized structures, respectively. Different active spaces are tested as reference for the successive calculations, and the results are compared to less expensive methods, such as DFT calculations using the B3LYP and B3PW91 functionals.

This setup allows a detailed discussion of the effect of nuclear motion on the synchronicity of the coupled electronic rearrangement and vice versa. Furthermore, it extends previous

quantum chemical data on the degenerate Cope rearrangement of semibullvalene, mostly relying on density functional theory,^{11–13,19,21,23,24,26} including an exploration of the underlying PES. The reader is referred to refs 24 and 25 for a calculation of the intrinsic reaction path at the B3LYP and CASSCF levels of theory, respectively, and also refs 35–38 for related quantum chemical treatments of the degenerate Cope rearrangement of 1,5-hexadiene and the review⁵⁶ emphasizing the necessity to use multiconfigurational methods including a high degree of dynamic electron correlation for a correct description of the transition state region. Finally, we extend the analysis of electronic fluxes associated with bond making and bond breaking, which relied on a partitioning of the total density due to unwanted contributions of rearranging CH bonds,^{21,23} and show that the major effects are already apparent in the total density when appropriate observer planes monitoring the electronic rearrangement are chosen.

■ COMPUTATIONAL DETAILS

The CASSCF and all successive calculations involving multi-reference methods (RS2, RS3, MRCISD+Dav) as well as CCSD(T) and B3LYP calculations are performed using the MOLPRO program package.⁴⁴ The DFT calculations using the B3PW91 functional are performed using the Gaussian suite of programs.⁵⁷ Dunning's correlation consistent basis sets⁴⁸ are used in all calculations.

Due to the competing valence structures of the HSS, c.f. Figure 1, it might be anticipated that both static and dynamic electron correlation effects need to be taken into account in order to give a balanced description of the PES for the Cope rearrangement of semibullvalene. For the static correlation effects and as reference space for successive MRCISD+Dav, RS2, and RS3 calculations, we test two different active spaces in the CASSCF calculations: In the first one (denoted CAS[4,4]), four electrons are distributed in orbitals $11a_1$, $5a_2$, $7b_1$, and $7b_2$ for the calculations of the HSS (C_{2v} -symmetry) and in orbitals $17a'$, $18a'$, $11a''$, and $12a''$ for calculations in C_s -symmetry. See Figure 1 for the orientation of the molecule. This choice of the active space allows the generation of the configuration state functions needed for a qualitatively correct description of the C_{2v} -cut through the PES at different interallylic distances R , i.e. $|...7b_17b_2|$ and $|...7b_25a_2|$ for large interallylic distances (bis-allyl-like structures), $|...7b_17b_2|$ for medium distances (bishomoaromatic structures), and finally $|...7b_17b_2|$ and $|...7b_111a_1|$ for short interallylic distances (3,7-diyl-like structures). See refs 35 and 36 for a corresponding analysis and ref 37 where CAS[4,4] has been identified as a promising reference for successive multireference calculations, both for the degenerate Cope rearrangement of 1,5-hexadiene. In the second choice of the active space (denoted CAS[6,6]), two electrons and orbitals $16a'$ and $13a''$ are added for the calculations in C_s -symmetry and orbitals $10a_1$ and $8b_2$ for those in C_{2v} -symmetry such that the active space in the latter case now consists of the three filled and three empty benzene-like molecular orbitals; see also refs 16 and 18. Figure S4 in the Supporting Information shows illustrations of the active orbitals in the respective symmetries (C_s and C_{2v}) for the two different active spaces used in this study. In the following, second order multireference perturbation theory calculations using the minimal reference active space will be denoted RS2[4,4] while those using the extended one are denoted RS2[6,6], with analogous expressions for the RS3 and MRCISD+Dav calculations.

Monitoring Electronic Motion. The number of electrons (electronic yield) flowing out of a given sector S_φ^{bb} during the pericyclic reaction shown as gray shaded area left of the center of mass in Figure 1 are associated with bond breaking (bb) in the following. This sector S_φ^{bb} is specified by the angle φ between the two half-planes A_φ^{bb} and \tilde{A}_φ^{bb} above and below the bridge of carbon atoms C_1/C_5 originating in the center of mass and forming the boundaries of the sector S_φ^{bb} . The electronic yields through either of these electronic observer planes A_φ^{bb} and \tilde{A}_φ^{bb} are, of course, identical due to the symmetric pincer motion type rearrangement of the electrons.⁴⁵ The corresponding sector S_φ^{bm} associated with bond making (bm) is also shown in Figure 1 right of the center of mass; see also Figure 3 for the respective sectors corresponding to $\varphi = 40^\circ$. Hence, the electronic yield associated with bond breaking along some reaction coordinate ξ from the reactant through the HSS to the product is given by

$$Y_\varphi^{bb}(\xi) = \underbrace{\int_{V_\varphi^{bb}} \rho_{el}(\mathbf{r}; \xi) dV}_{N_\varphi^{bb}(\xi)} - \underbrace{\int_{V_\varphi^{bb}} \rho_{el}(\mathbf{r}; \xi_{\text{reactant}}) dV}_{N_\varphi^{bb}(\xi_{\text{reactant}})} \quad (1)$$

Here, $N_\varphi^{bb}(\xi)$ denotes the number of electrons within sector S_φ^{bb} with volume V_φ^{bb} at specific values of the reaction coordinate ξ and is given by the corresponding volume integral over the one electron density $\rho_{el}(\mathbf{r}; \xi)$, with \mathbf{r} denoting the electronic coordinate. $N_\varphi^{bb}(\xi_{\text{reactant}})$ gives the corresponding electron number associated with the reactant. Analogous expressions hold for the electronic yield associated with bond making, $Y_\varphi^{bm}(\xi)$. The one electron density $\rho_{el}(\mathbf{r}; \xi)$ is evaluated at the respective quantum chemical level of theory on a spatial grid ($301 \times 301 \times 301$ grid point) centered at the center of mass with the axis corresponding to the principal axis of inertia. The equidistant step size is chosen as $\Delta x = \Delta y = \Delta z = 0.026 \text{ \AA}$. This approach may be considered as an approximation to the explicitly time-dependent treatment given in refs 21 and 23, neglecting effects of nuclear quantum dispersion, which has been shown to be a very reasonable approximation.²¹

RESULTS AND DISCUSSION

Exploring the PES for the Degenerate Cope Rearrangement of Semibullvalene. In order to investigate the effect of nuclear motion on the synchronicity of the pincer motion type electronic rearrangement associated with bond making and bond breaking and vice versa, c.f. Figure 1, different paths from the reactant over the respective potential barriers to the product are investigated. This includes a test both of the quantum chemical method and of the observer planes used to monitor the electronic rearrangement: Path a involves synchronous motion of all the nuclei, path b synchronous σ -bond elongation and σ -bond contraction with all other degrees of freedom optimized, and path c crosses the transition state, that is, the lowest energy HSS. Note that chemical reactions do not necessarily involve the transition state, especially when excited by selective laser pulses, see refs 58, 59 and refs 26, 60, 61, respectively.

Figure 2(a) shows the potential energy surfaces associated with path a (solid lines) and path b (dashed lines) for various quantum chemical methods (see the figure legend), using the cc-pVTZ basis sets as a function of the pericyclic coordinate ξ defined as the bond lengths difference of the old and new bond, $\xi = (C_{2y}-C_{8y}) - (C_{4y}-C_{6y})$,¹⁴ where C_{iy} denotes the y -component of the position vector of carbon atom i , c.f. Figure

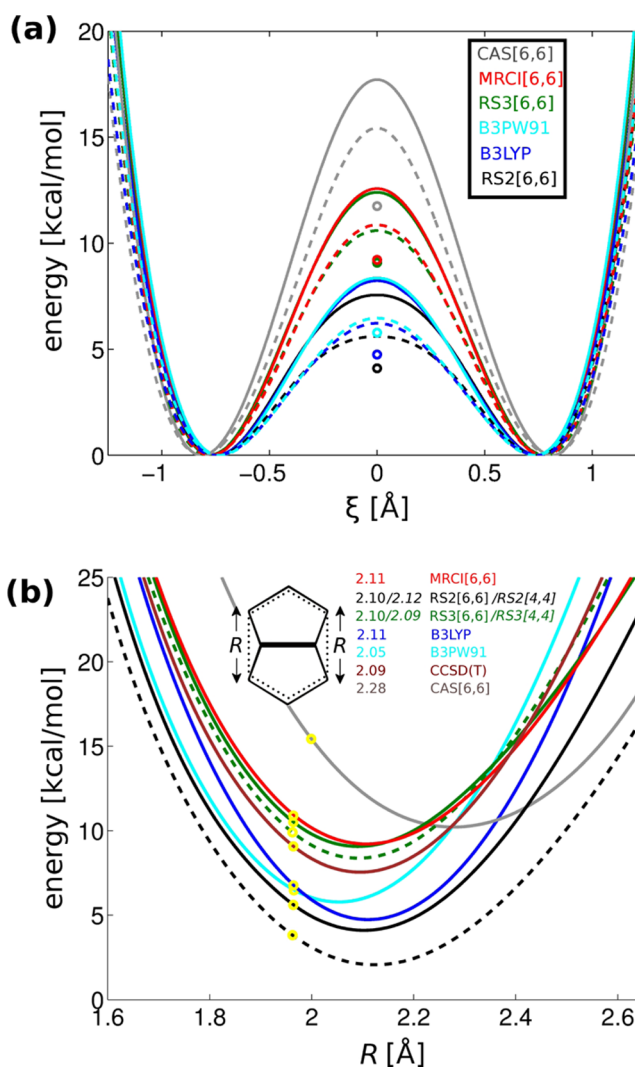


Figure 2. (a) Cuts through the potential energy surface for the degenerate Cope rearrangement of semibullvalene in C_s -symmetry at different levels of theory as function of the pericyclic coordinate ξ ; see the text for details and the legend for color coding. Solid lines correspond to path a involving synchronous motion of all the nuclei, and dashed lines to path b, corresponding to synchronous bond breaking and bond making of carbon atoms C_2/C_8 and C_4/C_6 , respectively, with all other degrees of freedom optimized. See Figure 1 for the labeling of the carbon atoms. Additionally shown are the minimum barrier heights involving asynchronous bond making and bond breaking as circles. (b) Corresponding cuts in C_{2v} -symmetry as a function of the interallylic distance R with energies relative to the respective global minima in C_s -symmetry. In addition to the methods shown in Figure 2(a), results are also shown for CCSD(T) (brown lines), RS2[4,4] (dashed dark lines), and RS3[4,4] (dashed green lines). The optimized values of R are given in the figure legend in Ångström and the interallylic distances and corresponding energies resulting from synchronous bond making and breaking (path b) are marked by yellow circles. All calculations used the cc-pVTZ basis sets; see also Table S1 in the Supporting Information for the numerical values of the respective barrier heights and a test of the basis set quality.

1. For path b, structure optimizations were carried out at various values for ξ at the CAS[6,6], B3LYP, B3PW91, and RS2[6,6] levels of theory, and the latter potential energy surface was refined by MRCISD[6,6]+Dav and RS3[6,6] single point calculations. Additionally, shown as circles are the minimum

barrier heights associated with the transition state at $\xi = 0$. We observe very good agreement between the RS3[6,6] and MRCISD[6,6]+Dav results shown as green and red lines, respectively. The associated barrier heights are significantly overestimated using solely the reference wave function (CAS[6,6], gray) and significantly underestimated using second order multireference perturbation theory (RS2[6,6], black). For numerical values of the respective barrier heights, see Table S1 in the Supporting Information. These deviations point to the importance of including a high degree of dynamic electron correlation; see refs 35–38 and 56 for analogous conclusions for the degenerate Cope rearrangement of 1,5-hexadiene. The experimental enthalpic barrier is $\Delta H = 4.8\text{--}5.2$ kcal/mol,^{4,7} pointing, at first glance, to excellent agreement with the DFT method B3LYP with corresponding barrier height $\Delta E = 4.75$ kcal/mol; see Table S1 (Supporting Information) and also refs 16 and 24. Considering, however, that inclusion of zero point energy effects and thermochemical corrections lower the barrier for the degenerate Cope rearrangement of semibullvalene by at least 1 kcal/mol,^{16,19} we see that the experimental barrier height is underestimated by B3LYP whereas the highly correlated wave function based methods (RS3[6,6], MRCISD[6,6]+Dav) approach the experimental result and excellent results are observed using the B3PW91 functional. The latter, however, is due to a fortitious cancellation of errors yielding altogether unsatisfactory results; see discussion of Figure 2(b). Increasing the quality of the basis set is expected to support the positive trend for the wave function based methods (see ref 38), while we observe rather well converged results for the DFT methods (see Table S1 (Supporting Information)). The optimized B3LYP, B3PW91, and RS2[6,6] structures for the reactant agree rather well among each other and to previously reported theoretical (see refs 16 and 19) and experimental³ results, whereas significant discrepancies for the $C_4\text{--}C_6$ bond-length are observed at the CAS[6,6] level; see Figure S2 in the Supporting Information for details. Hence, except for the CAS[6,6] method, virtually identical structures along path a are obtained since these depend only on the reactant (and product) structures, with similar results holding for path b; see Figure 3 for the optimized structures associated with the reactant and the respective HSS.

As anticipated, the quantum chemical description of the transition state region is much more involved. Figure 2(b) shows C_{2v} -cuts through the PES as function of the interallylic distance R for the same methods used in Figure 2(a), with energies relative to the reactant and the product. Additionally shown are RS2[4,4] optimizations (black dashed lines) as well as CCSD(T) single point calculations (brown solid lines) on RS2[6,6] optimized structures. The barrier heights associated with path b, that is, synchronous bond length elongation and contraction corresponding to the maxima of the dashed lines in Figure 2(a) at $\xi = 0$, are marked by yellow circles. The respective optimized values for the interallylic distance R are given in the figure legend in Ångström; see also the circles at $\xi = 0$ in Figure 2(a). Again, excellent agreement concerning both optimized structures and energies is observed for the RS3[6,6] and MRCISD[6,6]+Dav methods. This is rather nicely reproduced by the considerably less expensive RS3[4,4] calculations (green dashed lines), with the slight underestimation of the stability of the bis-allyl-like structures at large R -values in close resemblance to the CCSD(T) results. Neglecting an evidently important part of dynamic electron correlation, the RS2[6,6] and RS2[4,4] calculations consid-

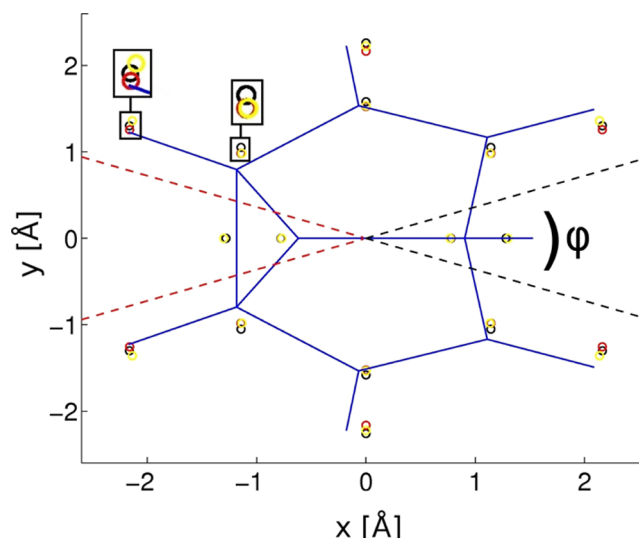


Figure 3. Bird's eye view along the z -axis, c.f. Figure 1, of the RS2[6,6]/cc-pVTZ optimized nuclear framework for the reactant structure (blue) including observer planes for electronic motion associated with bond breaking (red dashed lines) and bond making (black dashed lines) for the particular corridor width $\varphi = 40^\circ$. Additionally shown are the optimized positions of the carbon and hydrogen atoms for the transition state (black circles) and for the HSS associated with path a (yellow circles) and to path b (red circles) with blowups for carbon C_2 and the attached hydrogen indicated by black frames.

erably underestimate the respective barrier heights. However, both the optimized interallylic distance and the relative stabilities of the 3,7-diyl and bis-allyl-like structures at small and large interallylic distances, respectively, are very well described at the RS2[6,6] level of theory, while distinct deviations are observed at the RS2[4,4] level. The lower level methods B3PW91 and CAS[6,6] yield too small and too large optimized R -values, respectively, with corresponding unsatisfactory descriptions of the relative stabilities along the C_{2v} -cut. Finally, B3LYP gives an excellent optimized R -value while underestimating the relative stabilities of the bis-allyl and 3,7-diyl-like structures.

Concerning the one-electron basis, we find a systematic decrease of the optimized interallylic distance and the barrier heights upon increasing the basis-set quality in the case of the wave function based methods. The DFT methods merely show a slight decrease of the barrier heights around the optimized R -values while the latter remain constant. See Figure S3 in the Supporting Information for a comparison of the results obtained using the cc-pVDZ and cc-pVTZ basis-sets. In the following, the coupled electronic and nuclear rearrangement will be analyzed, and its sensitivity with respect to the described discrepancies of the electronic structure methods will be highlighted. The RS2[6,6] results serve as reference for the succeeding method comparison due to the demonstrated satisfactory description of the PES and since the actual barrier heights do not play a role in the conclusions that will be drawn in the following. Furthermore, results obtained solely with the cc-pVTZ basis sets will be presented.

Analyzing the Coupled Electronic and Nuclear Rearrangement. We begin the analysis of the electron–nuclear rearrangement by a qualitative discussion of the density differences $\Delta\rho_i(\mathbf{r}) = \rho_{\text{reactant}}(\mathbf{r}) - \rho_{\text{HSS},i}(\mathbf{r})$ at the RS2[6,6]/cc-pVTZ level where $\rho_{\text{reactant}}(\mathbf{r})$ is the one-electron density

corresponding to the reactant and $\rho_{\text{HSS},i}(\mathbf{r})$ with $i = a, b, c$ corresponds to the HSS associated with path (i), see Figure 4.

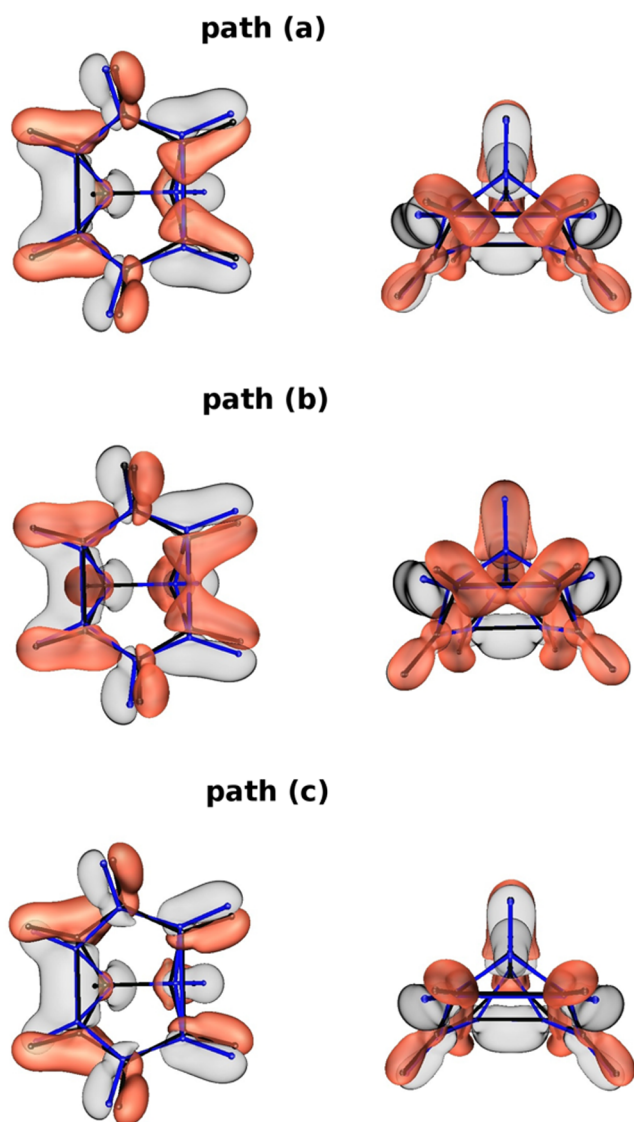


Figure 4. Isosurface plots of density differences between the reactant and three C_{2v} -structures at the RS2[6,6]/cc-pVTZ level of theory corresponding to path a (top), path b (middle), and path c (bottom); see text for details. Gray colors correspond to decreasing and red colors correspond to increasing densities with isosurface values of $0.03a_0^{-3}$ and $-0.03a_0^{-3}$, respectively. In each case, two perspectives are shown, on the left side the bird's eye view along the z -axis toward the carbon bridge C_1-C_5 and on the right side the front view along the negative x -axis; see Figure 1 for the orientation of the molecule and labeling of the carbon atoms. Additionally shown are the nuclear frameworks of the reactant (blue) and of the respective C_{2v} -structures (black). The program AMIRA was used for data visualization.⁶²

For better insight, two different perspectives of the isosurface plots are shown: The left columns correspond to bird's eye views toward the carbon bridge C_1-C_5 while the right columns show front views along the carbon bridge from the new toward the old σ -bond. Gray isosurfaces correspond to decreasing densities (e.g., bond breaking and initial positions of CH-bonds), and red isosurfaces correspond to increasing densities. Additionally shown are the nuclear frameworks corresponding to the reactant and to the respective HSS in blue and black,

respectively. For all paths considered, more pronounced bond breaking than bond making is observed on the way from the reactant to the respective barriers which is most evident for path c as a result of the underlying asynchronicity of σ -bond elongation and contraction. This asynchronicity of the electronic rearrangement is partly masked in the case of path b by the more pronounced motion of the hydrogens connected to carbon atoms C_4 and C_6 toward each other compared to the corresponding motion for paths a and c, while their counterparts connected to carbons C_2 and C_8 hardly move at all. These differences are also highlighted in Figure 3, which shows the nuclear framework of the reactant in blue as well as the nuclear positions of the HSS associated with path a (yellow), b (red), and c (black) using the same perspective as in the left column of Figure 4.

Figure 5(a) shows the corresponding quantitative results, that is, the number of electrons (electronic yields) flowing out of sector $S_{\varphi=40^\circ}^{\text{bb}}$ associated with bond breaking and into sector $S_{\varphi=40^\circ}^{\text{bm}}$ associated with bond making from the reactant ($\xi = -1.41 \text{ \AA}$) over the respective HSS ($\xi = 0$) to the product ($\xi = 1.41 \text{ \AA}$). See also Figure 3 for a plot of the specific sectors $S_{\varphi=40^\circ}^{\text{bb}}$ (red dashed lines) and $S_{\varphi=40^\circ}^{\text{bm}}$ (black dashed lines). The results for bond breaking (solid lines) and bond making (dashed lines) are shown both for the rearrangement of the total electron density $\rho_{\text{el}}(\mathbf{r};\xi)$ (black) and for the valence density $\rho_{\text{el, val}}(\mathbf{r};\xi) = \rho_{\text{el}}(\mathbf{r};\xi) - \rho_{\text{el, core}}(\mathbf{r};\xi)$ (red), where $\rho_{\text{el, core}}(\mathbf{r};\xi)$ accounts for the 16 core electrons associated with the 8 carbon 1s shells. In spite of the synchronous σ -bond elongation and σ -bond contraction along ξ , both for path a (upper panel) and path b (lower panel), more pronounced electronic flux out of the old bond than into the new bond is observed on the way from the reactant to the respective HSS. This is, of course, reversed on the remaining path to the product due to the underlying symmetry of the reaction. This asynchronicity is quantized by the parameter $\alpha(\varphi) = Y_{\varphi}^{\text{bb}}(\xi = 0) - Y_{\varphi}^{\text{bm}}(\xi = 0)$, c.f. eq 1 and the upper panel in Figure 5(a), and is apparent both in the total and in the valence density. Note that the slightly diminished yields for the total density are due to the motion of the carbon bridge C_1-C_5 into S_{φ}^{bb} and out of S_{φ}^{bm} , respectively, thereby counteracting the inversely directed electronic fluxes associated with bond breaking and bond making. Hence, in Figure 5(b), which shows the asynchronicity parameter α as function of the sector width φ for paths a, b, and c, at various levels of theory, we focus solely on the valence density. For all paths, a clear asynchronicity of the electronic rearrangement is apparent at all levels of theory, which is enhanced for path c due to more pronounced σ -bond elongation compared to σ -bond contraction from the reactant to the transition state, see Figure 2(b). We note that α increases up to sector widths of roughly $\varphi = 40^\circ$ and then decreases. Hence, sector widths $\varphi < 40^\circ$ are apparently well suited to monitor electronic rearrangement associated with σ -bond making and breaking, c.f. Figure 4, while sectors with widths $\varphi > 40^\circ$ monitor, for example, rearrangement of CH bonds and electronic density close to the carbon atoms. The former is particularly evident in the case of path b, for which the already discussed more pronounced motion of the CH bonds into sector S_{φ}^{bm} , c.f. Figure 2(c) and middle panel of Figure 4, leads to an inversion of the asynchronicity. The latter is, however, not observed when contributions of CH bonds are filtered out; see the analysis in terms of localized orbitals (Figure 6). For paths a and b, we observe very good agreement between all quantum chemical methods except for CAS[6,6]. This is due to the

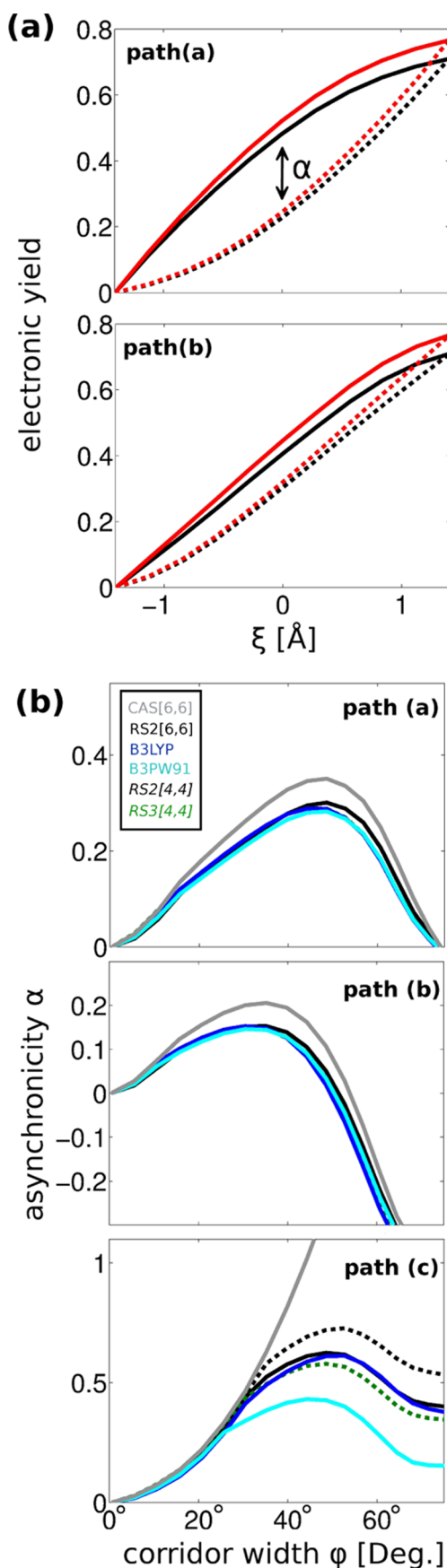


Figure 5. (a) Number of total electrons (black) and valence electrons (red) leaving sector $S_{\varphi=40^\circ}^{bb}$ associated with bond breaking (solid lines) and entering sector $S_{\varphi=40^\circ}^{bm}$ associated with bond making (dashed lines)

Figure 5. continued

as function of the pericyclic coordinate ξ when going from the reactant ($\xi = -1.41$ Å) via the C_{2v} -structure ($\xi = 0$) to the product ($\xi = 1.41$ Å) for path a (top panel) and path b (bottom panel) calculated using the RS2[6,6]/cc-pVTZ method; see Figure 3 for a plot of these sectors corresponding to $\varphi = 40^\circ$. (b) Asynchronicity α of bond making and bond breaking as defined in part (a) as function of the width of the observer sectors φ for path a (top), path b (middle), and path c (bottom) for the valence density. The results are shown at different levels of theory: CAS[6,6] (gray), RS2[6,6] (black), B3LYP (blue), B3PW91 (cyan), RS2[4,4] (dashed black lines), and RS3[4,4] (dashed green lines).

insensitivity of the one-electron densities computed for identical nuclear structures with respect to different levels of theory, and to virtually identical nuclear structures along paths a and b, except for CAS[6,6]. For the latter method, the longer C_4-C_6 bond for the reactant, c.f. Figure S2 (Supporting Information), leads to an artificial increase of the asynchronicity α . For path c, however, the asynchronicities are much more sensitive with respect to the quantum chemical level of theory since they depend strongly on the interallylic distance R of the transition state. We observe very good agreement between the RS2[6,6] (black solid lines) and B3LYP (blue solid lines) methods, which is rather well reproduced by RS3[4,4] (green dashed lines), while RS2[4,4] (black dashed lines) and especially CAS[6,6] (gray solid lines) overestimate the optimized R -values, c.f. Figure 2(b), and hence the asynchronicity α . Finally, B3PW91 (cyan solid lines) underestimates the interallylic distance and thus the asynchronicity of the electronic rearrangement.

To filter out, in large part, spurious contributions, for example, of rearranging CH groups, the B3LYP valence density is partitioned further by transformation into localized orbitals using the Pipek-Mezey method.⁶³ Three localized orbitals accounting for the six rearranging electrons according to the Lewis structures are identified along the respective paths; see also refs 21 and 23. These three localized orbitals build up the so-called pericyclic density that represents the shifting σ -like and π -like bonds; see Figure 6(a) for isosurface plots of this pericyclic density for the reactant (left), the HSS at three different interallylic distances R (middle), and the product (right) corresponding nicely to the chemical picture anticipated from Figure 1. The comparison between the asynchronicity α as a function of the sector width φ of the pericyclic density (green) and the valence density (blue) for path a (dashed lines), path b (dashed-dotted lines), and path c (solid lines) is given in Figure 6(b). We see nicely how the hitherto weak asynchronicity for path b in terms of the valence density, c.f. middle panel in Figure 5(b), is significantly enhanced in the case of the pericyclic density due to considerable reduction of contributions from CH bonds, yielding now comparable results to path a. For the latter, the asynchronicity is slightly enhanced when the analysis is done in terms of the pericyclic density because the yields associated with bond breaking, Y_{φ}^{bb} , c.f. eq 1, are significantly enhanced, while Y_{φ}^{bm} is less affected when contributions from the rearranging C_1-C_5 -bridge and associated hydrogens are reduced, with similar results for path c in the case of small sector widths φ . For larger widths, however, the asynchronicity for path c in terms of the pericyclic density is decreased compared to results obtained using the valence density, since for this path the consideration of

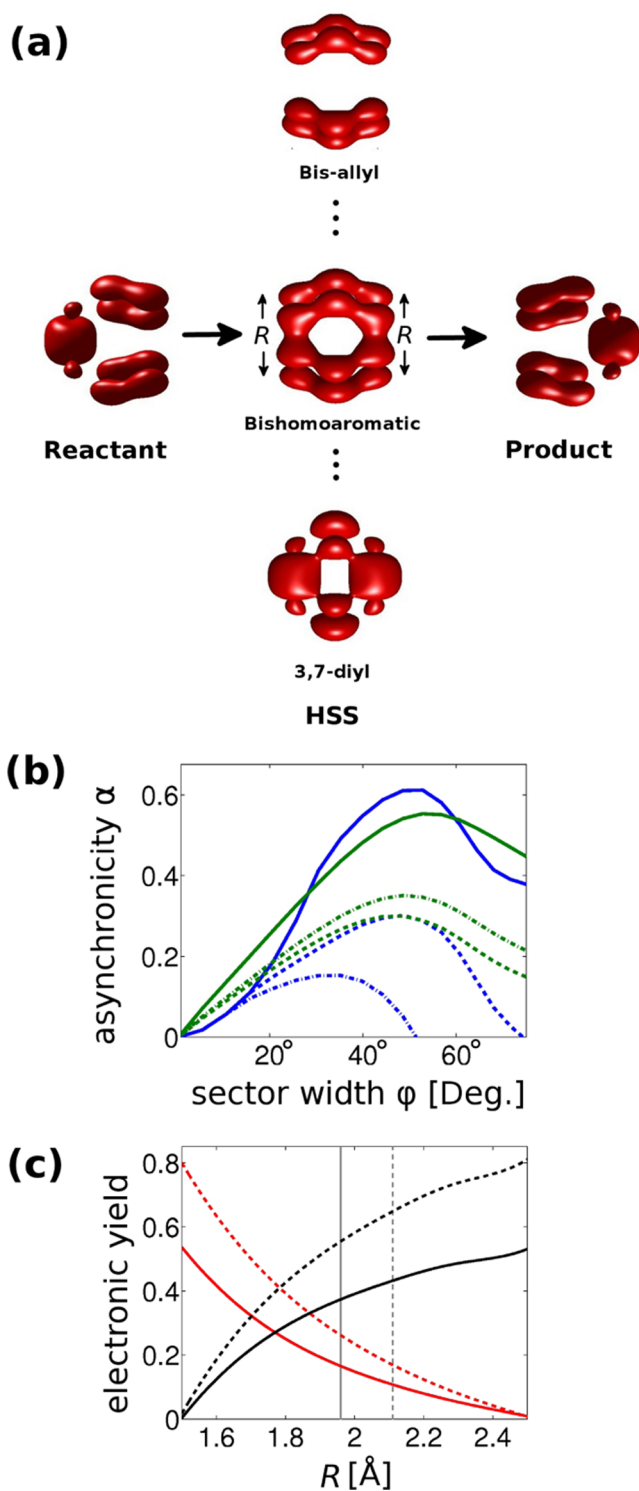


Figure 6. (a) Isosurface plot of the pericyclic density consisting of three localized orbitals and accounting for six rearranging electrons in the six-membered carbon ring shown for reactant (left), product (right), and for the high symmetry species (HSS, middle) at three different interallylic distances. The isosurface value is $0.03a_0^{-3}$. (b) Asynchronicity α , c.f. Figure 5, as function of the corridor width for path a (dashed lines), path b (dashed-dotted lines), and path c (solid lines) for the pericyclic density (green). For comparison, the results are also shown for the valence density (blue lines, c.f. Figure 5(b)). (c) Number of pericyclic electrons leaving sector S_{ϕ}^{bb} associated with bond breaking (black) and entering sector S_{ϕ}^{bm} associated with bond making (red) as function of the interallylic distance R from the reactant to the respective HSS for corridor widths $\phi = 25^\circ$ (solid lines) and $\phi = 40^\circ$

Figure 6. continued

(dashed lines). Solid gray vertical lines mark the interallylic distance associated with synchronous σ -bond elongation and contraction and dashed gray vertical lines mark the optimized R -values, c.f. Figure 2(b). The results were obtained at the B3LYP/cc-pVTZ level of theory.

hydrogens connected to carbon atoms involved in σ -bond breaking and making enhances α due to the underlying asynchronous nuclear rearrangement.

Finally, we analyze the effect of synchronous electronic rearrangement on the nuclear motion: Figure 6(c) shows the electronic yield associated with bond breaking (black) and bond making (red) for the pericyclic density from the reactant to various HSS characterized by the interallylic distance R for sector widths $\phi = 25^\circ$ (solid lines) and $\phi = 40^\circ$ (dashed lines), illustrating nicely the asynchronicity of the electron–nuclear motion: Synchronous electronic rearrangement is observed at $R = 1.78$ Å, marked by the crossings of the respective black and red curves, and is rather insensitive to the sector width ϕ . On the other hand, synchronous nuclear motion corresponding to path b is marked by the vertical gray solid line at $R = 1.96$ Å. Hence, synchronous electronic fluxes out of the old and into the new bond occur for paths along the PES involving asynchronous nuclear rearrangement, that is, more pronounced σ -bond contraction compared to σ -bond elongation from the reactant to the HSS with short interallylic distances corresponding to 3,7-diyl-like structures. Paths involving the transition state, on the other hand, which are marked by the vertical gray dashed dotted line, show more pronounced σ -bond elongation compared to contraction from the reactant to the transition state and, hence, a large asynchronicity of the electronic rearrangement with the asynchronicity parameter α given by the gap between the respective red and black curves in Figure 6(c).

SUMMARY

The quantum chemical analysis presented in this study shows, by exploring various paths along the potential energy surface at different levels of theory, that the coupled electronic and nuclear rearrangement associated with bond making and bond breaking in the degenerate Cope rearrangement of semi-bullvalene occurs asynchronously. In particular, we explored three paths from the reactant over the respective potential barriers to the product: Path a involves synchronous motion of all the nuclei, path b is characterized by synchronous elongation and contraction of the old bond and new bond, respectively, including relaxation of all remaining degrees of freedom, and path c leads over the transition state involving asynchronous σ -bond elongation and contraction. In all cases, the associated pincer-motion type rearrangement of the electron density common to pericyclic reactions occurring in nondegenerate electronic states, for example, the electronic ground state,⁴⁵ c.f. Figure 1, involves stronger electronic flux out of the old bond compared to electronic flux into the new bond from the reactant to the respective barrier, quantified by the asynchronicity parameter α (Figure 5). These electronic flux patterns are, of course, reversed along the remaining path to the product due to the underlying symmetry of the reaction. On the other hand, synchronous electronic rearrangement associated with bond making and bond breaking entails asynchronous σ -bond elongation and contraction involving 3,7-diyl-like structures (Figure 6(c)). These asynchronicities are

stable with respect to the quantum chemical method and to the observer surfaces used to monitor the electronic motion.

In particular, we performed full structure optimizations including a scan of the PES as a function of the interallylic distance R (Figure 2(b)) up to the RS2 level of theory using the cc-pVTZ basis sets and a reference wave function consisting of six active electrons in six active orbitals (RS2[6,6]). These optimizations were subsequently refined at the RS3[6,6], MRCISD[6,6]+Dav, and CCSD(T) levels of theory. The calculations were tested against analogous, less expensive calculations using a reference wave function containing four active electrons in four active orbitals, and to DFT calculations using the B3LYP and B3PW91 functionals. For the description of the reactant and product, except for the CAS[6,6] calculations, excellent agreement between the tested methods among each other and to available experimental data is observed. The quantitative description of the transition state region, however, requires taking into account a high degree of both static and dynamic electron-correlation, and excellent agreement is observed solely at the MRCISD[6,6]+Dav and RS3[6,6] levels of theory (Figure 2). The essential features of the PES, especially the optimized value for the interallylic distance R and the involved description of the relative stabilities of the bis-allyl and 3,7-diyl-like structures along the C_{2v} -cut through the PES, however, are well described at the RS2[6,6] level of theory, while the actual barrier heights associated with the different paths are considerably underestimated compared to the MRCISD[6,6]+Dav and RS3[6,6] methods. Increasingly better values for the barrier heights are obtained by the B3LYP, CCSDT(T), and RS3[4,4] methods, while, despite excellent optimized R -values, the relative stabilities along the C_{2v} -cut are less well described by these methods. Finally, the RS2[4,4], B3PW91, and CAS[6,6] methods give increasingly less accurate descriptions of the underlying PES for the degenerate Cope rearrangement of semibullvalene.

The electronic yields are insensitive with respect to the quantum chemical method used for the computation of the one-electron densities for specific nuclear structures such that the results for the electronic rearrangement associated with bond making and bond breaking depend solely on the nuclear structures along the respective paths. Hence, due to the excellent agreement for the optimized reactant and product structures for all methods used (except for CAS[6,6]), analogous excellent agreement is observed in the description of the coupled electronic and nuclear rearrangement along path a, c.f. Figure 5(b), with equivalent results for path b. For the latter path, an analysis in terms of localized orbitals turned out to be essential to gain chemical insight due to the necessity to reduce contributions of e.g. rearranging CH groups.

The appropriate description of the asynchronicity of the electronic motion associated with path c relies on an accurate description of the optimized interallylic distance R such that the asynchronicity is considerably overestimated by the CAS[6,6] method and underestimated using the B3PW91 method while good results are obtained using B3LYP. We note, however, that, for example, simulations of the coherent control of the underlying process (see, e.g., refs 64 and 65) rely on an accurate description of the complete transition state region, that is, of the bis-allyl, bishomoaromatic and 3,7-diyl-like structures, and therefore require the usage of highly correlated methods, such as RS3[6,6]. Work along these lines is in progress.

■ ASSOCIATED CONTENT

■ Supporting Information

Barrier heights of the degenerate Cope rearrangement of semibullvalene associated with paths a, b, and c using different basis sets (Table S1). Optimized structures at the B3LYP, B3PW91, RS2[6,6], and CAS[6,6] levels of theory using the cc-pVTZ basis sets for the reactant as well as for the transition state including comparison to experimental results (Figure S2). Comparison between cc-pVDZ and cc-pVTZ basis sets for cuts through the potential energy surface in C_{2v} -symmetry as function of the interallylic distance R at various levels of theory (Figure S3). Illustration of the active orbitals for the calculations in C_s symmetry and in C_{2v} symmetry for the two different active spaces used in this study (Figure S4). This information is available free of charge via the Internet at <http://pubs.acs.org/>.

■ AUTHOR INFORMATION

Corresponding Author

*E-mail: bredt@chemie.fu-berlin.de.

Notes

The authors declare no competing financial interest.

■ ACKNOWLEDGMENTS

We thank Prof. J. Manz and Dr. J. C. Tremblay (Freie Universität Berlin) for valuable and stimulating discussions. The computing facilities (ZEDAT) of the Freie Universität Berlin are acknowledged for computer time, and we thank Deutsche Forschungsgemeinschaft (DFG, project Ma 515/25-1) for financial support.

■ REFERENCES

- (1) Zimmerman, H. E.; Grunewald, G. L. *J. Am. Chem. Soc.* **1966**, *88*, 183–184.
- (2) Zimmerman, H. E.; Binkley, R. W.; Givens, R. S.; Grunewald, G. L.; Sherwin, M. A. *J. Am. Chem. Soc.* **1969**, *91*, 3316–3323.
- (3) Wang, Y. C.; Bauer, S. H. *J. Am. Chem. Soc.* **1972**, *94*, 5651–5657.
- (4) Cheng, A. K.; Anet, F. A. L.; Mioduski, J.; Meinwald, J. *J. Am. Chem. Soc.* **1974**, *96*, 2887–2891.
- (5) Christoph, G. G.; Beno, M. A. *J. Am. Chem. Soc.* **1978**, *100*, 3156–3163.
- (6) Quast, H.; Christ, J. *Angew. Chem., Int. Ed.* **1984**, *23*, 631–632.
- (7) Moskau, D.; Aydin, R.; Leber, W.; Günther, H.; Quast, H.; Martin, H.-D.; Hassenrück, K.; Miller, L. S.; Grohmann, K. *Chem. Ber.* **1989**, *122*, 925–931.
- (8) Quast, H.; Seefelder, M. *Angew. Chem., Int. Ed.* **1999**, *38*, 1064–1067.
- (9) Seefelder, M.; Quast, H. *Angew. Chem., Int. Ed.* **1999**, *38*, 1068–1071.
- (10) Williams, R. V. *Chem. Rev.* **2001**, *101*, 1185–1204.
- (11) Goren, A. C.; Hrovat, D. A.; Seefelder, M.; Quast, H.; Borden, W. T. *J. Am. Chem. Soc.* **2002**, *124*, 3469–3472.
- (12) Seefelder, M.; Heubes, M.; Quast, H.; Edwards, W. D.; Armantrout, J. R.; Williams, R. V.; Cramer, C. J.; Goren, A. C.; Hrovat, D. A.; Borden, W. T. *J. Org. Chem.* **2005**, *70*, 3437–3449.
- (13) Griffiths, P. R.; Pivonka, D. E.; Williams, R. V. *Chem.—Eur. J.* **2011**, *17*, 9193–9199.
- (14) Bergmann, K.; Goertler, S.; Manz, J.; Quast, H. *J. Am. Chem. Soc.* **1993**, *115*, 1490–1495.
- (15) Dohle, M.; Manz, J.; Paramonov, G. K.; Quast, H. *Chem. Phys.* **1995**, *197*, 91–97.
- (16) Jiao, H.; Nagelkerke, R.; Kurtz, H. A.; Williams, R. V.; Borden, W. T.; von Ragué Schleyer, P. *J. Am. Chem. Soc.* **1997**, *119*, 5921–5929.

- (17) Zilberg, S.; Haas, Y.; Danovich, D.; Shaik, S. *Angew. Chem., Int. Ed.* **1998**, *37*, 1394–1397.
- (18) Brown, E. C.; Henze, D. K.; Borden, W. T. *J. Am. Chem. Soc.* **2002**, *124*, 14977–14982.
- (19) Brown, E. C.; Bader, R. F. W.; Werstiuk, N. H. *J. Phys. Chem. A* **2009**, *113*, 3254–3265.
- (20) Zhang, X.; Hrovat, D. A.; Borden, W. T. *Org. Lett.* **2010**, *12*, 2798–2801.
- (21) Andrae, D.; Barth, I.; Bredtmann, T.; Hege, H.-C.; Marquardt, F.; Paulus, B. *J. Phys. Chem. B* **2011**, *115*, 5476–5483.
- (22) Greve, D. R. *J. Phys. Org. Chem.* **2011**, *24*, 222–228.
- (23) Bredtmann, T.; Manz, J. *Angew. Chem., Int. Ed.* **2011**, *50*, 12652–12654.
- (24) González-Navarrete, P.; Andrés, J.; Berski, S. *J. Phys. Chem. Lett.* **2012**, *3*, 2500–2505.
- (25) Ichikawa, Y.; Sakai, S. *J. Phys. Org. Chem.* **2012**, *25*, 409–419.
- (26) Bredtmann, T.; Manz, J. *J. Chem. Sci.* **2012**, *124*, 121–129.
- (27) Zewail, A. H. *Angew. Chem., Int. Ed.* **2000**, *39*, 2586–2631.
- (28) Krausz, F.; Ivanov, M. *Rev. Mod. Phys.* **2009**, *81*, 163–234.
- (29) *Quantum Dynamics Imaging*; CRM Series in Mathematical Physics; Bandrauk, A., Ivanov, M., Eds.; Springer: New York, 2011.
- (30) Bredtmann, T.; Chelkowski, S.; Bandrauk, A. D. *J. Phys. Chem. A* **2012**, *116*, 11398–11405.
- (31) Wernet, P. *Phys. Chem. Chem. Phys.* **2011**, *13*, 16941–16954.
- (32) Stolow, A. *Annu. Rev. Phys. Chem.* **2003**, *54*, 89–119.
- (33) Bredtmann, T.; Chelkowski, S.; Bandrauk, A. D. *Phys. Rev. A* **2011**, *84*, 021401.
- (34) Gajewski, J. *Acc. Chem. Res.* **1980**, *13*, 142–148.
- (35) Staroverov, V. N.; Davidson, E. R. *J. Am. Chem. Soc.* **2000**, *122*, 7377–7385.
- (36) Staroverov, V. N.; Davidson, E. R. *THEOCHEM* **2001**, *573*, 81–89.
- (37) Ventura, E.; Andrade do Monte, S.; Dallos, M.; Lischka, H. *J. Phys. Chem. A* **2003**, *107*, 1175–1180.
- (38) McGuire, M. J.; Piecuch, P. *J. Am. Chem. Soc.* **2005**, *127*, 2608–2614.
- (39) Dewar, M. J. S. *J. Am. Chem. Soc.* **1984**, *106*, 209–219.
- (40) Borden, W. T.; Loncharich, R. J.; Houk, K. N. *Annu. Rev. Phys. Chem.* **1988**, *39*, 213–236.
- (41) Houk, K. N.; Li, Y.; Evanseck, J. D. *Angew. Chem., Int. Ed.* **1992**, *31*, 682–708.
- (42) Xu, L.; Doubleday, C. E.; Houk, K. N. *J. Am. Chem. Soc.* **2010**, *132*, 3029–3037.
- (43) Black, K.; Liu, P.; Xu, L.; Doubleday, C.; Houk, K. N. *Proc. Natl. Acad. Sci. U.S.A.* **2012**, DOI: 10.1073/pnas.1209316109.
- (44) Werner, H.-J.; Knowles, P. J.; Knizia, G.; Manby, F. R.; Schütz, M.; Celani, P.; Korona, T.; Lindh, R.; Mitrushenkov, A.; Rauhut, G.; Shamasundar, K. R.; Adler, T. B.; Amos, R. D.; Bernhardsson, A.; Berning, A.; Cooper, D. L.; Deegan, M. J. O.; Dobbyn, A. J.; Eckert, F.; Goll, E.; Hampel, C.; Hesselmann, A.; Hetzer, G.; Hrenar, T.; Jansen, G.; Köppl, C.; Liu, Y.; Lloyd, A. W.; Mata, R. A.; May, A. J.; McNicholas, S. J.; Meyer, W.; Mura, M. E.; Nicklaß, A.; O'Neill, D. P.; Palmieri, P.; Peng, D.; Pflüger, K.; Pitzer, R.; Reiher, M.; Shiozaki, T.; Stoll, H.; Stone, A. J.; Tarroni, R.; Thorsteinsson, T.; Wang, M. *MOLPRO*, version 2012.1, a package of ab initio programs; 2012. Available online: www.molpro.net.
- (45) Manz, J.; Yamamoto, K. *Mol. Phys.* **2012**, *110*, 517–530.
- (46) Becke, A. D. *J. Chem. Phys.* **1993**, *98*, 5648–5652.
- (47) Lee, C.; Yang, W.; Parr, R. G. *Phys. Rev. B* **1988**, *37*, 785–789.
- (48) Dunning, T. H. *J. Chem. Phys.* **1989**, *90*, 1007–1023.
- (49) Werner, H.-J. *Mol. Phys.* **1996**, *89*, 645–661.
- (50) Celani, P.; Werner, H.-J. *J. Chem. Phys.* **2003**, *119*, 5044–5057.
- (51) Werner, H.-J.; Knowles, P. J. *J. Chem. Phys.* **1988**, *89*, 5803–5814.
- (52) Knowles, P. J.; Werner, H.-J. *Chem. Phys. Lett.* **1988**, *145*, 514–522.
- (53) Langhoff, S. R.; Davidson, E. R. *Int. J. Quantum Chem.* **1974**, *8*, 61–72.
- (54) Werner, H.-J.; Knowles, P. J. *J. Chem. Phys.* **1985**, *82*, 5053–5063.
- (55) Knowles, P. J.; Werner, H.-J. *Chem. Phys. Lett.* **1985**, *115*, 259–267.
- (56) Borden, W. T.; Davidson, E. R. *Acc. Chem. Res.* **1996**, *29*, 67–75.
- (57) Frisch, M. J.; Trucks, G. W.; Schlegel, H. B.; Scuseria, G. E.; Robb, M. A.; Cheeseman, J. R.; Scalmani, G.; Barone, V.; Mennucci, B.; Petersson, G. A.; Nakatsuji, H.; Caricato, M.; Li, X.; Hratchian, H. P.; Izmaylov, A. F.; Bloino, J.; Zheng, G.; Sonnenberg, J. L.; Hada, M.; Ehara, M.; Toyota, K.; Fukuda, R.; Hasegawa, J.; Ishida, M.; Nakajima, T.; Honda, Y.; Kitao, O.; Nakai, H.; Vreven, T.; Montgomery, J. A., Jr.; Peralta, J. E.; Ogliaro, F.; Bearpark, M.; Heyd, J. J.; Brothers, E.; Kudin, K. N.; Staroverov, V. N.; Kobayashi, R.; Normand, J.; Raghavachari, K.; Rendell, A.; Burant, J. C.; Iyengar, S. S.; Tomasi, J.; Cossi, M.; Rega, N.; Millam, J. M.; Klene, M.; Knox, J. E.; Cross, J. B.; Bakken, V.; Adamo, C.; Jaramillo, J.; Gomperts, R.; Stratmann, R. E.; Yazyev, O.; Austin, A. J.; Cammi, R.; Pomelli, C.; Ochterski, J. W.; Martin, R. L.; Morokuma, K.; Zakrzewski, V. G.; Voth, G. A.; Salvador, P.; Dannenberg, J. J.; Dapprich, S.; Daniels, A. D.; Farkas, O.; Foresman, J. B.; Ortiz, J. V.; Cioslowski, J.; Fox, D. J. *Gaussian 09*, Revision A.1; Gaussian Inc.: Wallingford, CT, 2009.
- (58) Hartke, B.; Manz, J. *J. Am. Chem. Soc.* **1988**, *110*, 3063–3068.
- (59) Townsend, D.; Lahankar, S. A.; Lee, S. K.; Chembreau, S. D.; Suits, A. G.; Zhang, X.; Rheinecker, J.; Harding, L. B.; Bowman, J. M. *Science* **2004**, *306*, 1158–1161.
- (60) Iwakura, I.; Yabushita, A.; Kobayashi, T. *Chem. Lett.* **2010**, *39*, 374–375.
- (61) Iwakura, I.; Yabushita, A.; Liu, J.; Okamura, K.; Kobayashi, T. *Phys. Chem. Chem. Phys.* **2012**, *14*, 9696–9701.
- (62) Stalling, D.; Westerhoff, M.; Hege, H. C. In *The Visualization Handbook*; Hansen, C. D., Johnson, C. R., Eds.; Elsevier: Amsterdam, 2005; Chapter 38, pp 749–767.
- (63) Pipek, J.; Mezey, P. G. *J. Chem. Phys.* **1989**, *90*, 4916–4926.
- (64) Shapiro, M.; Brumer, P. *Quantum Control of Molecular Processes*, 2nd ed.; Wiley-VCH: Weinheim, 2005.
- (65) Daniel, C.; Full, J.; González, L.; Lupulescu, C.; Manz, J.; Merli, A.; Vajda, S.; Wöste, L. *Science* **2003**, *299*, 536–539.